Simulations of real-time system identification for superconducting cavities with a recursive least-squares algorithm

Volker Ziemann[*]

Uppsala University, 75120 Uppsala, Sweden

We explore the performance of a recursive least-squares algorithm to determine the bandwidth ω_{12} and the detuning $\Delta\omega$ of a superconducting cavity. We base the simulations on the parameters of the European Spallation Source double-spoke cavities. Expressions for the signal-to-noise ratio of derived parameters are given to explore the applicability of the algorithm to other configurations.

I. INTRODUCTION

Superconducting accelerating cavities are used to accelerate protons [1,2], electrons [3–5], and heavy ions [6–8], both with pulsed [1,4] and with continuous beams [3,9]. Owing to the low losses, the cavities have a very narrow bandwidth on the order of Hz for bare cavities and a few 100 Hz for cavities equipped with high-power couplers. In order to efficiently cool these cavities with liquid helium, they are made of rather thin material that makes them easily deformable and this changes their resonance frequency, often by an amount comparable to their bandwidth. In pulsed operation, the dominant deformation comes from the electromagnetic pressure of the field inside the cavity, the Lorentz-force detuning [10,11], while cavities operating continuously are perturbed by so-called microphonics [12,13], caused by pressure variations of the liquid helium bath or mechanical perturbations, for example, by reciprocating pumps or by malfunctioning equipment. As a consequence of these perturbations, the cavities are detuned and force the power generators to increase their output to maintain fields necessary for the stable operation of the beams. This reduces the efficiency of the system and requires an, often substantial, overhead of the power generation, forcing it to operate at a less than optimal working point. To avoid this suboptimal mode of operation and to compensate for the detuning, many accelerators employ active tuning systems that use stepper motors and piezo-actuators [14] to squeeze the cavities back in tune, which requires diagnostic systems to measure the detuning. These measurements are usually based on comparing the phase of the signal that excites the cavity, measured with a directional coupler just upstream of the input coupler, to the phase of the field inside the cavity, measured by a field probe or antenna inside the cavity. Both analog [12,15] and digital [16,17] signal processing systems are used; often as part of the low-level radio-frequency (LLRF) feedback system that stabilizes the fields in the cavity. Even more elaborate systems, based on various system identification algorithms, are used or planned [18–21]. All these algorithms normally rely on low-pass filtering of the often noisy signals from the directional couplers and antennas in order to provide a reliable estimate of the cavity detuning and the bandwidth.

In this report, we focus on a complementary algorithm that continuously improves the estimated fit parameters by increasing the size of a system of equations. Instead of solving this rapidly growing system directly, we employ a recursive least-squares (RLS) algorithm [22,23], which only requires moderate numerical expenditure in each time step. Remarkably, asymptotically the difference between the continuously improving estimates of the fit parameters and the "true" values—the so-called estimation error—approaches zero [24] albeit at the expense of a limited ability to resolve changing parameters. We therefore introduce a finite memory when solving the system, which downgrades old measurements in favor of new ones. This allows us to handle even changing parameters at the expense of an increased noise level of the fit parameters.

In the following sections, we first introduce the model of the cavity and transform the continuous-time model to discrete time. In Sec. III, we develop the RLS algorithm to identify the cavity parameters. In Sec. IV, we explore the capabilities of the algorithm in simulations before calculating the signal-to-noise ratio in Sec. V and the conclusions.

II. MODEL

Accelerating cavities can be described by an equivalent circuit composed of a resistor R, an inductance L, and a capacitor C, all connected in parallel. This circuit is then excited by a current I and responds by building up a voltage

[*]Corresponding author: volker.ziemann@physics.uu.se

$V = V_r + iV_i$ across the components. This voltage is decomposed into real (in-phase, I) and imaginary (out-of-phase, Q) components. After averaging over the fast oscillations, the evolution of the real and imaginary parts of the voltage envelope is given by the following state-space representation [16]

$$
\begin{pmatrix} \frac{dV_r}{dt} \\ \frac{dV_i}{dt} \end{pmatrix} = \begin{pmatrix} -\omega_{12} & -\Delta\omega \\ \Delta\omega & -\omega_{12} \end{pmatrix} \begin{pmatrix} V_r \\ V_i \end{pmatrix}
$$
$$
+ \begin{pmatrix} \omega_{12}R & 0 \\ 0 & \omega_{12}R \end{pmatrix} \begin{pmatrix} I_r \\ I_i \end{pmatrix} \tag{1}
$$

of the system that describes the dynamics of the cavity voltage powered by a generator that provides the currents. The directional couplers used to measure the input signal, however, measure the forward component of the current $\vec{I}^+$ rather than the total current $\vec{I} = \vec{I}^+ + \vec{I}^-$. Close to resonance, it is straightforward to show that the measured forward current $\vec{I}^+$, which is proportional to the signal from the directional coupler, is related to the total current $\vec{I}$ by

$$
\vec{I} = \frac{2\beta}{1+\beta}\vec{I}^+ = \frac{2Q_L}{Q_E}\vec{I}^+ \tag{2}
$$

with the coupling factor $\beta = Q_0/Q_E$ given by the ratio of the intrinsic quality factor of the cavity Q_0 and the external quality factor Q_E. Moreover, $1/Q_L = 1/Q_0 + 1/Q_E = (1+\beta)/Q_0$ defines the loaded quality factor Q_L. Replacing the currents on the right-hand side of Eq. (1) with the help of Eq. (2), then leads to

$$
\begin{pmatrix} \frac{dV_r}{dt} \\ \frac{dV_i}{dt} \end{pmatrix} = \begin{pmatrix} -\omega_{12} & -\Delta\omega \\ \Delta\omega & -\omega_{12} \end{pmatrix} \begin{pmatrix} V_r \\ V_i \end{pmatrix} + \begin{pmatrix} \omega_E R & 0 \\ 0 & \omega_E R \end{pmatrix} \begin{pmatrix} I_r^+ \\ I_i^+ \end{pmatrix} \tag{3}
$$

with $\omega_E = \hat{\omega}/Q_E$. We also introduce $\omega_{12} = \hat{\omega}/2Q_L$ and the cavity resonance frequency $\hat{\omega}$. Furthermore, we assume that the magnitude and phase of all currents and voltages can be reliably measured after the hardware (antennas, cables, and amplifiers) is properly calibrated. Equation (3) is in the standard form of a linear dynamical system $\dot{\vec{V}} = \bar{A}\,\vec{V} + \bar{B}\vec{I}^+$ where $\vec{V}$ is the column vector with the real and imaginary part of the voltages and $\vec{I}^+$ that of the forward currents. The matrices $\bar{A}$ and $\bar{B}$ correspond to those in Eq. (3) and are given by

$$
\bar{A} = \begin{pmatrix} -\omega_{12} & -\Delta\omega \\ \Delta\omega & -\omega_{12} \end{pmatrix} \quad \text{and} \quad \bar{B} = \begin{pmatrix} \omega_E R & 0 \\ 0 & \omega_E R \end{pmatrix}. \tag{4}
$$

For the simulations, we will convert the continuous-time system from Eq. (3) to discrete time with time step Δt,

which corresponds to the sampling time if the system is implemented digitally. By replacing the derivatives of the voltages with finite differences

$$
\frac{d\vec{V}}{dt} \rightarrow \frac{\vec{V}_{t+1} - \vec{V}_t}{\Delta t}, \tag{5}
$$

where we label the time steps by t, Eq. (3) becomes

$$
\vec{V}_{t+1} = A\vec{V}_t + B\vec{I}_t^+ + \vec{w}_t \quad \text{with}
$$
$$
A = \begin{pmatrix} 1 - \omega_{12}\Delta t & -\Delta\omega\Delta t \\ \Delta\omega\Delta t & 1 - \omega_{12}\Delta t \end{pmatrix}, \tag{6}
$$

$B = \omega_E \Delta t R\mathbf{1}$, and the process noise $\vec{w}_t$. We assume that the noise is uncorrelated and has magnitude σ_p. It is thus characterized by its expectation value $E\{\vec{w}_t\vec{w}_s^\top\} = \sigma_p^2\delta_{ts}\mathbf{1}$. We add measurement noise $\vec{w}_t'$ by using

$$
\vec{V}_t' = \vec{V}_t + \vec{w}_t' \tag{7}
$$

in the system identification process. We assume it is uncorrelated, has magnitude σ_m, and is characterized by $E\{\vec{w}_t'\vec{w}_s'^\top\} = \sigma_m^2\delta_{ts}\mathbf{1}$.

III. SYSTEM IDENTIFICATION

Now we turn to the task of extracting $\omega_{12}\Delta t$ and $\Delta\omega\Delta t$ from continuously measured voltages $\vec{V}_t'$ and currents $\vec{I}_t^+$. In order to isolate the sought parameters, we rewrite Eq. (6) in the form

$$
\vec{V}_{t+1}' = (\mathbf{1}+F)\vec{V}_t' + B\vec{I}_t^+ \quad \text{with} \quad F = \begin{pmatrix} -\omega_{12}\Delta t & -\Delta\omega\Delta t \\ \Delta\omega\Delta t & -\omega_{12}\Delta t \end{pmatrix} \tag{8}
$$

and $B = \omega_E \Delta t R\mathbf{1}$. After reorganizing this equation to

$$
\vec{V}_{t+1}' - \vec{V}_t' - B\vec{I}_t^+ = F\vec{V}_t' \tag{9}
$$

we rewrite $F\vec{V}_t'$ on the right-hand side as

$$
F\vec{V}_t' = -\omega_{12}\Delta t \begin{pmatrix} V_r' \\ V_i' \end{pmatrix}_t + \Delta\omega\Delta t \begin{pmatrix} -V_i' \\ V_r' \end{pmatrix}_t
$$
$$
= \begin{pmatrix} -V_r' & -V_i' \\ -V_i' & V_r' \end{pmatrix}_t \begin{pmatrix} \omega_{12}\Delta t \\ \Delta\omega\Delta t \end{pmatrix}. \tag{10}
$$

We now introduce the abbreviations

$$
G_t = \begin{pmatrix} -V_r' & -V_i' \\ -V_i' & V_r' \end{pmatrix}_t \quad \text{and} \quad \vec{y}_{t+1} = \vec{V}_{t+1}' - \vec{V}_t' - B\vec{I}_t^+ \tag{11}
$$

and stack Eq. (9) for consecutive times on top of each other. In this way, we obtain a growing system of equations to determine $\omega_{12}\Delta t$ and $\Delta\omega\Delta t$

$$\begin{pmatrix} \vec{y}_2 \\ \vec{y}_3 \\ \vdots \\ \vec{y}_{T+1} \end{pmatrix} = U_T \begin{pmatrix} \omega_{12}\Delta t \\ \Delta \omega \Delta t \end{pmatrix} \quad \text{with} \quad U_T = \begin{pmatrix} G_1 \\ G_2 \\ \vdots \\ G_T \end{pmatrix} \qquad (12)$$

that we solve in the least-squares sense with the Moore-Penrose pseudoinverse [25]

$$\vec{q}_T = \begin{pmatrix} \omega_{12}\Delta t \\ \Delta \omega \Delta t \end{pmatrix}_T = (U_T^\top U_T)^{-1} U_T^\top \begin{pmatrix} \vec{y}_2 \\ \vec{y}_3 \\ \vdots \\ \vec{y}_{T+1} \end{pmatrix}. \qquad (13)$$

Here we introduce the abbreviation $\vec{q}_T$ to denote the estimated parameters at time step T.

We can avoid lengthy evaluations by calculating Eq. (13) recursively. With the definition $P_T^{-1} = U_T^\top U_T$, its initial value $P_0 = p_0\mathbf{1}$, and the definition of U_T from Eq. (12), we express P_{T+1} through P_T in the following way:

$$\begin{aligned} P_{T+1}^{-1} &= U_{T+1}^\top U_{T+1} \\ &= p_0\mathbf{1} + G_1^\top G_1 + G_2^\top G_2 + \cdots + G_T^\top G_T + G_{T+1}^\top G_{T+1} \\ &= P_T^{-1} + G_{T+1}^\top G_{T+1}. \end{aligned} \qquad (14)$$

We note that for all time steps t

$$G_t^\top G_t = (V_r'^2 + V_i'^2)_t \mathbf{1} = \vec{V}_t'^2 \mathbf{1} \qquad (15)$$

is proportional to the unit matrix $\mathbf{1}$. This renders the fit into two orthogonal and independent parts; one for each of the fit parameters. To proceed, we introduce the scalar quantity p_T with $P_T = p_T\mathbf{1}$ and find that it obeys

$$p_{T+1}^{-1} = p_T^{-1} + \vec{V}_T'^2. \qquad (16)$$

Taking the reciprocal leads to

$$p_{T+1} = \left[\frac{1}{1 + p_T \vec{V}_T'^2} \right] p_T. \qquad (17)$$

Note that we need to initialize this recursion with a nonzero value and set $p_0 = 1$ in the simulations. Despite being numerically unity, we carry p_0 through all equations, because it carries the inverse units of $\vec{V}_T^2$.

We now turn to finding $\vec{q}_{T+1}$ by writing Eq. (13) for $T + 1$

$$\begin{aligned} \vec{q}_{T+1} &= p_{T+1}(G_1^\top \vec{y}_2 + G_2^\top \vec{y}_3 + \cdots + G_T^\top \vec{y}_{T+1} + G_{T+1}^\top \vec{y}_{T+2}) \\ &= \left[\frac{1}{1 + p_T \vec{V}_T'^2} \right] p_T \left(\sum_{t=1}^{T} G_t^\top \vec{y}_{t+1} + G_{T+1}^\top \vec{y}_{T+2} \right) \\ &= \left[\frac{1}{1 + p_T \vec{V}_T'^2} \right] (\vec{q}_T + p_T G_{T+1}^\top \vec{y}_{T+2}). \end{aligned} \qquad (18)$$

Equations (17) and (18) constitute the algorithm to continuously update estimates for the two components of $\vec{q}$, the bandwidth $q(1) = \omega_{12}\Delta t$, and the detuning $q(2) = \Delta\omega\Delta t$, as new voltage and current measurements—both enter in G_{T+1} and $\vec{y}_{T+2}$—become available. We refer to the MATLAB [26] code on github [27] for the details of the implementation.

In Eqs. (17) and (18), new information from measurements are used to continuously improve the estimate of the fit parameters, but in situations where they change, we have to introduce a way to forget old information. Therefore, in order to emphasize newly added information, we follow [22,28] and introduce a "forgetting factor" $\alpha = 1 - 1/N_f$ where N_f is the time horizon over which old information is downgraded in the last equality of Eq. (14), which now reads

$$P_{T+1}^{-1} = \alpha P_T^{-1} + G_{T+1}^\top G_{T+1}. \qquad (19)$$

We see that we only have to replace P_T by P_T/α, or equivalently p_T by p_T/α, in the derivation of Eqs. (17) and (18) and find for the update of p_T

$$p_{T+1} = \left[\frac{1}{\alpha + p_T \vec{V}_T'^2} \right] p_T \qquad (20)$$

and for the update of the estimated parameters $\vec{q}_T$

$$\vec{q}_{T+1} = \left[\frac{1}{\alpha + p_T \vec{V}_T'^2} \right] (\alpha \vec{q}_T + p_T \hat{G}_{T+1}^\top \vec{y}_{T+2}) \qquad (21)$$

that are capable of following time-dependent system parameters. These expressions can be evaluated very efficiently. We find that the calculations in Eq. (20) involve four multiplications and one inverse, whereas the calculations in Eq. (21) involve ten multiplications if we reuse the expression in the square bracket. Thus, in total, 14 multiplication and one, computationally more expensive, inverse are required. This is about 10 times the computational effort needed for a proportional integral (PI) controller that typically requires three multiplications. The processing delay of the system identification algorithm should therefore be correspondingly longer. The details of the timing depend of course on the hardware used to implement these algorithms. In particular, on a field-programmable gate array, many operations can be done in parallel.
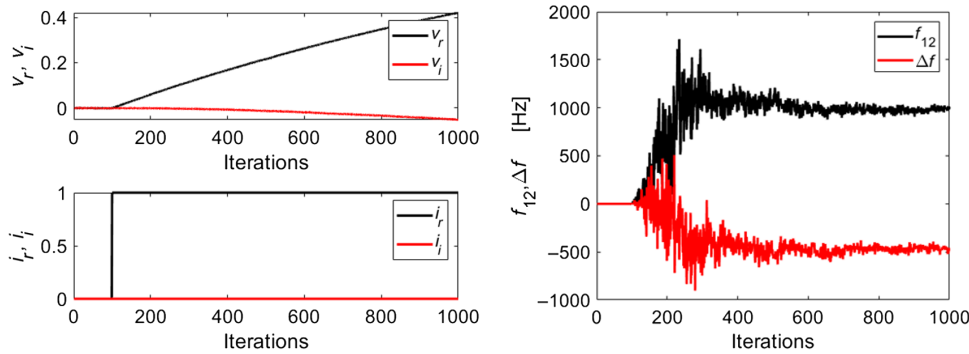
FIG. 1.   Left: the normalized currents (bottom) and the voltages (top) after starting to fill the cavity for 1000 iterations (100 μs). Right: the reconstructed fit parameters, the bandwidth f_{12} (black), and the detuning Δf (red). Note that the parameters are found despite the noise level ($\sigma_p = 10^{-4}$ and $\sigma_m = 10^{-3}$ of peak voltage) used in the simulation.

IV. SIMULATIONS

We base our simulations on parameters for the prototype spoke-cavity module [29] for the European Spallation Source [2], which operates at 352 MHz, has an external Q_E [30] in the range of 1.75×10^5–2.85×10^5. One of the measured cavities exhibited a loaded Q of $Q_L = 1.8 \times 10^5$ [31] while it was operating at a high gradient. The resulting bandwidth is $f_{12} = \omega_{12}/2\pi \approx 1000$ Hz. The cavity showed Lorentz-force detuning on the order of a few hundred Hz [31–33]; for our simulations, we typically use $\Delta f = \Delta\omega/2\pi = 500$ Hz. Moreover, we use a process noise level of $\sigma_p = 10^{-4} \times V_{\max}$ and a measurement noise level of $\sigma_m = 10^{-3} \times V_{\max}$, where $V_{\max}$ is the peak voltage inside the cavity. We report the voltages and currents normalized to the values without detuning and denote them by v_r, v_i and i_r, i_i, respectively. The peak voltage and current in those conditions then become unity. Furthermore, we assume that the data-acquisition system operates at a rate of 10 Msamples/s, resulting in $\Delta t = 100$ ns. We found that the forgetting horizon N_f scales with the relative noise levels σ_p and σ_m. We use $N_f = 100$, unless explicitly specified, because it gave good results.

The left-hand side in Fig. 1 shows the normalized currents and voltages over the first 1000 iterations (100 μs), where the currents are turned on after 100 iterations. We observe that the real part of the current (black line) assumes its new value at that point, whereas the imaginary part (red line) stays zero. The voltages, shown on the upper panel slowly starts rising as the cavity is filled. Even the imaginary part of the voltage deviates from zero, owing to the finite value of the detuning. The right-hand side of Fig. 1 shows the fit parameters $f_{12} = \omega_{12}/2\pi$ and $\Delta f = \Delta\omega/2\pi$ over the same 1000 iterations. We observe that during the first few hundred iterations, the estimated fit parameters are very noisy but settle on their correct value after this initial period. After about iteration 600, they meander quite closely around their "true" values.

We can understand this behavior by noting that p_T is proportional to the diagonal element of the empirical covariance matrix $P_T = (U_T^\top U_T)^{-1}$ of the least-squares fit in Eq. (13). Therefore the square root of p_T is proportional to the error bars of the fit parameter. Figure 2 shows p_T for a simulation with $N_f = 100$ (black solid) and $N_f = 10$ (red dashes) for 5000 iterations. We observe that both curves initially increase during the period that the fit is noisy but then approach a constant value that determines the achievable error bars of the fit parameters. This value can be derived from Eq. (20) by setting $p_{T+1} = p_T = p_\infty$ and solving for $p_\infty = 1/N_f \vec{V}'^2_\infty$. Here $\vec{V}'_\infty$ is the voltage inside the cavity. For the error bars of both components of $\vec{q}$, we thus find $\sigma_m/\sqrt{N_f \vec{V}'^2_\infty}$, a value that corresponds to the rms deviations of the fit parameters, shown, for example, on the second half in Fig. 1. Furthermore, by construction, the off-diagonal elements of the matrix $P_T = p_T \mathbf{1}$ are zero, which indicates that the fit of the bandwidth and the detuning are orthogonal and that makes the algorithm very robust. Moreover, we found that instead of operating an open loop, using a PI-controller to control
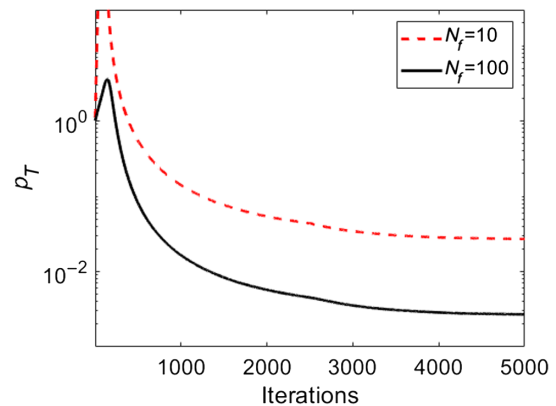
FIG. 2.   The variable p_T as a function of the iterations for $N_f = 100$ (solid) and $N_f = 10$ (dashes).
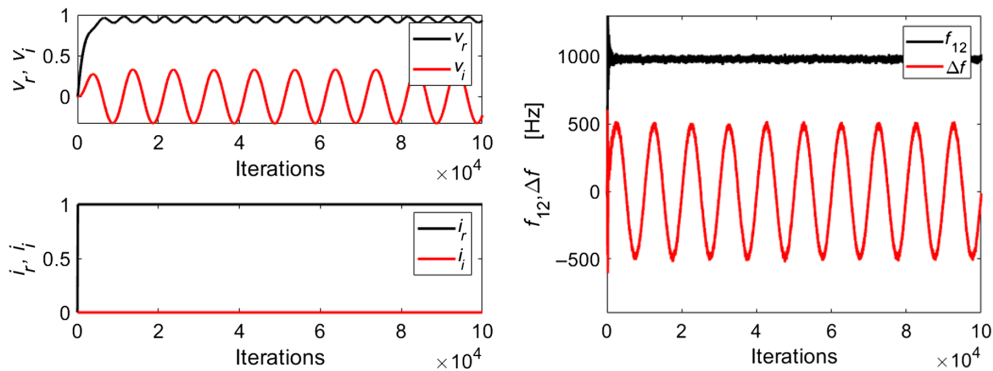
FIG. 3.　The currents and voltages (left) and the fit parameters (right) for 10^5 iterations (10 ms) while the detuning Δf oscillates with an amplitude of 500 Hz and with a mechanical-mode frequency of 1 kHz. The oscillations are clearly visible on both phases of the voltage and the correctly reconstructed fit parameters.

the cavity voltage does not significantly alter the performance of the system identification process.

We now explore the algorithm's ability to identify parameter changes during steady state operation. The left-hand side in Fig. 3 illustrates the effect of microphonics on the currents and voltages. We simulate this by an oscillation of Δf with an amplitude of $f_{12}/2$ and frequency of 1 kHz. Especially v_i reveals this oscillation, though also v_r oscillates. The right-hand side of Fig. 3 shows how the algorithm correctly identifies f_{12} and both the amplitude and oscillation frequency of Δf.

Increasing the oscillation frequency to 20 kHz results in Fig. 4 where we have reduced the duration of the simulation to 10^4 iterations in order to improve the visibility of oscillations on the plot. We see that the oscillations are still resolved, albeit at a lower amplitude, which is a consequence of the forgetting horizon $N_f = 100$. It implicitly introduces averaging over N_f iterations and thus behaves like a low-pass filter with a time constant of $N_f \Delta t = 10$ μs or a cutoff frequency on the order of
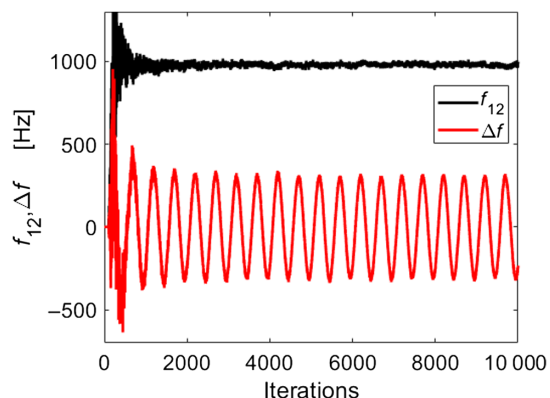
FIG. 4.　The reconstructed fit parameters for a 20-kHz mechanical oscillation of the detuning Δf. The oscillations are still seen, but the amplitude is significantly reduced. This can be partially alleviated by decreasing N_f, albeit at the expense of an increased noise level.

100 kHz that already causes some attenuation of the 20-kHz oscillation.

In Fig. 5, we explore a rapid increase of the bandwidth, for example, due to a quench. In the simulation, we simply double the value of ω_{12} after 5000 iterations. The plots in the top left of Fig. 5 show the currents and voltages and on the top right the fit parameters. We find that the fitted bandwidth (black) is indeed doubled and that the reconstruction of the detuning is unaffected. The plot on the bottom-left shows an enlarged view of the fit parameters around the time of the step. It shows that the doubled value is approached within about $2 \times N_f = 200$ iterations. If we run the same simulation with a 10 times reduced value of $N_f = 10$, we obtain the plot on the bottom right. We find that the changed value is approached within a few tens of iterations, albeit at the expense of an increased noise level, which is consistent with the discussion regarding Fig. 2. Balancing the noise level and the response is just a matter of adjusting the value of N_f, the topic of the following section.

V. SIGNAL TO NOISE

In Sec. IV, we already found that the asymptotic noise level N for constant parameters is given by

$$N = \frac{1}{\sqrt{N_f}} \frac{\sigma_m}{V'_\infty}, \tag{22}$$

where we denote the magnitude of $\vec{V}'_\infty$ by V'_∞. We now consider a situation where the system has reached a quasistationary state and that perturbations of the ω_{12} and $\Delta\omega$ are so small that they affect V'_∞ very little. We can therefore also use it to write $p_\infty = 1/N_f V'^2_\infty$ despite temporally varying ω_{12} and $\Delta\omega$. Replacing p_T by p_∞ in Eq. (21) then leads to

$$\vec{q}_{T+1} = \alpha\vec{q}_T + \frac{1}{N_f V'^2_\infty} G^\top_{T+1} \vec{y}_{T+2}. \tag{23}$$
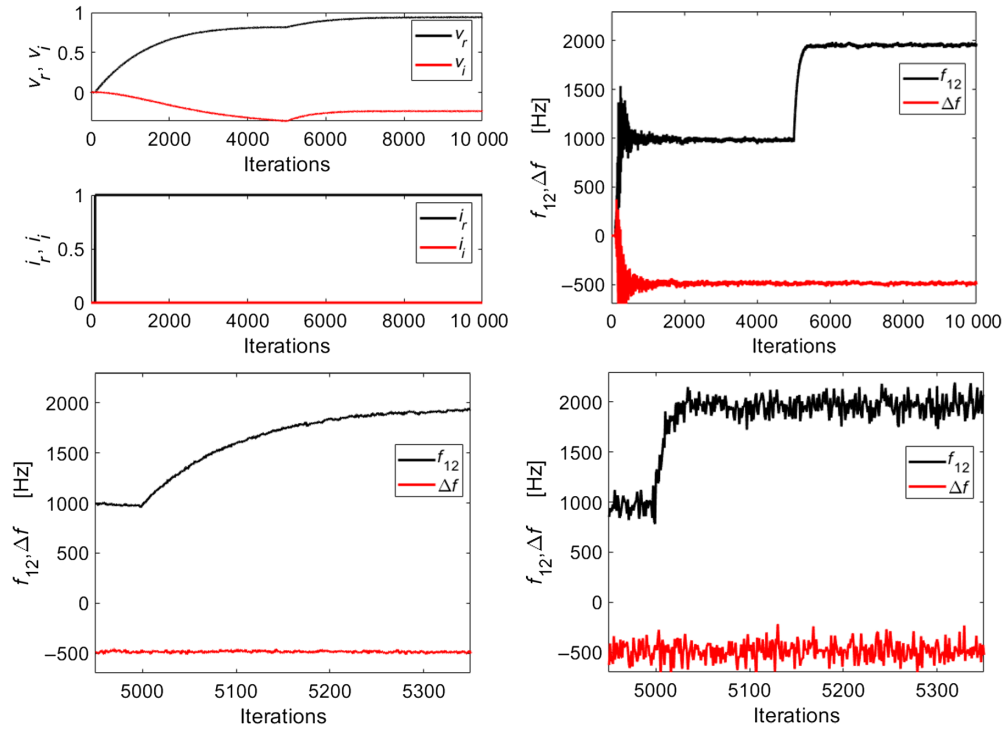
FIG. 5.   The currents and voltages (top left) and fit parameters (top right) for 10^4 iterations (1 ms) as the bandwidth f_{12} is doubled at iteration 5000. The bottom row shows an enlarged view of fit parameters around the time of the change. On the left, we use $N_f = 100$ and on the right, we use $N_f = 10$.

Using Eqs. (9) and (10), we rewrite $\vec{y}_{T+2}$ as

$$\vec{y}_{T+2} = G_{T+1} \begin{pmatrix} \omega_{12}\Delta t \\ \Delta\omega\Delta t \end{pmatrix}_{hw}, \tag{24}$$

where the vector on the right-hand side with the subscript *hw* are the "true" values of the hardware. Combining these equations, utilizing Eq. (15), and replacing V'_T by V'_∞, we arrive at

$$\vec{q}_{T+1} = \alpha\vec{q}_T + \frac{1}{N_f} \begin{pmatrix} \omega_{12}\Delta t \\ \Delta\omega\Delta t \end{pmatrix}_{hw}. \tag{25}$$

In the next step, we use $\alpha = 1 - 1/N_f$ and reshuffle terms to obtain

$$\frac{\vec{q}_{T+1} - \vec{q}_T}{\Delta t} = -\frac{1}{N_f\Delta t}\vec{q}_T - \frac{1}{N_f\Delta t}\begin{pmatrix} \omega_{12}\Delta t \\ \Delta\omega\Delta t \end{pmatrix}_{hw}. \tag{26}$$

Introducing $\tau_f = N_f\Delta t$, replacing the finite difference by a differential, and Laplace-transforming the resulting equation, we find

$$\left(s + \frac{1}{\tau_f}\right)\tilde{\vec{q}} = \frac{1}{\tau_f}\begin{pmatrix} \tilde{\omega}_{12}\Delta t \\ \Delta\tilde{\omega}\Delta t \end{pmatrix}_{hw}, \tag{27}$$

where s is the Laplace variable and we denote the Laplace transform of a variable by a tilde. We obtain the time dependence by replacing $s = i\omega = 2\pi i f$

$$\tilde{\vec{q}} = \frac{1}{1 + i\omega\tau_f}\begin{pmatrix} \tilde{\omega}_{12}\Delta t \\ \Delta\tilde{\omega}\Delta t \end{pmatrix}_{hw} \tag{28}$$

and find that the reconstructed system parameters $\tilde{\vec{q}}$ are given by the hardware parameters passed through a low-pass filter with time constant τ_f.

Of particular interest is the absolute value of the amplitude of the detuning $\Delta\tilde{\omega}$ at frequency ω, which is given by

$$S = \Delta\tilde{\omega} = \frac{\Delta\tilde{\omega}_{hw}}{\sqrt{1 + (\omega\tau_f)^2}}. \tag{29}$$

This constitutes the signal we strive to measure. For the signal-to-noise ratio S/N, we then find

$$S/N = \frac{\Delta\tilde{\omega}_{hw}}{\sqrt{1 + (2\pi N_f f\Delta t)^2}}\frac{\sqrt{N_f}}{(\sigma_m/V'_\infty)}, \tag{30}$$

where all parameters are explicitly written out in order to explore the tradeoff among them. Apparently, it depends

not only on the magnitude (amplitude) of the detuning $\Delta\tilde{\omega}_{hw}$ and the relative accuracy of the voltage measurement σ_m/V'_∞ but also on the attenuation of an oscillation due to the forgetting time horizon N_f. As long as S/N is sufficiently large, say 5 or so, the oscillation is discernible.

VI. CONCLUSIONS

We worked out an algorithm to determine the cavity bandwidth f_{12} and the detuning Δf by correlating the signal from a directional coupler before the cavity and the voltages inside the cavity. The calculations are very efficient and given by Eqs. (17) and (18) for static parameters and by Eqs. (20) and (21) for time-varying parameters. These recursion equations are very compact and require only moderate resources, for example, on a field-programmable gate array.

Despite the absence of low-pass filtering, the RLS algorithm is resilient to noise of the measured voltages, because the forgetting horizon implicitly introduces a low-pass filter whose time constant is $\tau_f = N_f \Delta t$. We can tailor the performance by selecting a large value of N_f, which reduces the noise of the reconstructed parameters, whereas smaller values of N_f make the algorithm more responsive to parameter changes on faster timescales. The tradeoff between achievable frequency resolution, N_f, and measurement noise σ_m can be explored with the help of Eq. (30).

[1] S. Henderson *et al.*, The Spallation Neutron Source accelerator system design, Nucl. Instrum. Methods Phys. Res., Sect. A **763**, 610 (2014).

[2] A. Jansson *et al.*, The status of the ESS project, in *Proceedings of IPAC 2022, Bangkok* (JACoW, Geneva, Switzerland, 2022), p. 792.

[3] B. Norum, J. McCarthy, and R. York, CEBAF—a high-energy, high duty factor electron accelerator for nuclear physics, Nucl. Instrum. Methods Phys. Res., Sect. B **10–11**, 337 (1985).

[4] W. Decking *et al.*, A MHz-repetition-rate hard X-ray free-electron laser driven by a superconducting linear accelerator, Nat. Photonics **14**, 391 (2020).

[5] A. Bartnik, N. Banerjee, D. Burke, J. Crittenden, K. Deitrick, J. Dobbins *et al.*, CBETA: First multipass superconducting linear accelerator with energy recovery, Phys. Rev. Lett. **125**, 044803 (2020).

[6] P. Ostroumov *et al.*, Beam commissioning in the first superconducting segment of the Facility for Rare Isotope Beams, Phys. Rev. Accel. Beams **22**, 080101 (2019).

[7] H. Goutte and A. Navin, Microscopes for the physics at the Femtoscale: GANIL-SPIRAL2, Nucl. Phys. News **31**, 5 (2021).

[8] W. Barth *et al.*, Advanced basic layout of the HElmholtz LInear ACcelerator for cw heavy ion beams at GSI, in *Proceedings of 14th International Particle Accelerator Conference, IPAC-2023, Venice, Italy* (JACoW, Geneva, Switzerland, 2023), 10.18429/JACoW-IPAC2023-TUPA186.

[9] C. Behre *et al.*, First lasing of the IR upgrade FEL at Jefferson lab, Nucl. Instrum. Methods Phys. Res., Sect. A **528**, 19 (2004).

[10] B. Aune *et al.*, Superconducting TESLA cavities, Phys. Rev. ST Accel. Beams **3**, 092001 (2000).

[11] O. Kononenko, C. Adolphsen, Z. Li, C. Ng, and C. Rivetta, 3D multiphysics modeling of superconducting cavities with a massively parallel simulation suite, Phys. Rev. Accel. Beams **20**, 102001 (2017).

[12] G. Davis *et al.*, Microphonics testing of the CEBAF upgrade 7-cell cavity, in *Proceedings of the 19th Particle Accelerator Conference, Chicago, IL, 2001* (IEEE, Piscataway, NJ, 2001), p. 1152.

[13] A. Neumann, W. Anders, O. Kugeler, and J. Knobloch, Analysis and active compensation of microphonics in continuous wave narrow-bandwidth superconducting cavities, Phys. Rev. ST Accel. Beams **13**, 082001 (2010).

[14] M. Liepe, Superconducting multicell cavities for linear colliders, Ph.D. thesis, Universität Hamburg, 2001.

[15] T. Powers, Theory and practice of cavity RF test systems, in *Proceedings of the 12th International Workshop on RF Superconductivity, Cornell University, Ithaca, NY* (LEPP, Cornell University, 2007), p. 30.

[16] T. Schilcher, Vector sum control of pulsed accelerating fields in Lorentz force detuned superconducting cavities, Ph.D. thesis, Universität Hamburg, 1998.

[17] T. Plawski *et al.*, Digital cavity resonance monitor-alternative way to measure cavity microphonics, in *Proceedings of the 12th International Workshop on RF Superconductivity, Cornell University, Ithaca, NY* (LEPP, Cornell University, 2007), p. 616.

[18] R. Rybaniec *et al.*, Real-time estimation of superconducting cavities parameters, in *Proceedings of the 5th International Particle Accelerator Conference, IPAC-2014, Dresden, Germany* (EPS-AG, Dresden, 2014), p. 2456.

[19] T. Czarski, Superconducting cavity control based on system model identification, Meas. Sci. Technol. **18**, 2328 (2007).

[20] A. Bellani *et al.*, Online detuning computation and quench detection for superconducting resonators, IEEE Trans. Nucl. Sci. **68**, 385 (2021).

[21] P. Echevarria, B. Arruabarrena, A. Ushakov, J. Jugo, and A. Neumann, Simulation of quench detection algorithms for Helmholtz Zentrum Berlin SRF cavities, in *Proceedings of the 10th International Particle Accelerator Conference, Melbourne, Australia* (JACoW, Geneva, Switzerland, 2019), p. 2834.

[22] K. Åström and B. Wittenmark, *Adaptive Control* (Dover Publications, Mineola, 2008); especially Sec. II.2.

[23] I. Ziemann and V. Ziemann, Noninvasively improving the orbit-response matrix while continuously correcting the orbit, Phys. Rev. Accel. Beams **24**, 072804 (2021).

[24] T. Lai and C. Wei, Least squares estimates in stochastic regression models with applications to identification and control of dynamic systems, Ann. Stat. **10**, 154 (1982).

[25] R. Penrose, A generalized inverse for matrices, Math. Proc. Cambridge Philos. Soc. **51,** 406 (1955).

[26] Mathworks web site at www.mathworks.com.

[27] Github repository for the software accompanying this report: https://github.com/volkziem/SysidRFcavity.

[28] V. Ziemann, Operational improvements for an algorithm to noninvasively measure the orbit response matrix in storage rings, arXiv:2303.11216.

[29] P. Duchesne, S. Bousson, S. Brault, P. Duthil, G. Olry, D. Reynet, and S. Molloy, Design of the 352 MHz, beta 0.50, double-spoke cavity for ESS, in *Proceedings of SRF2013, Paris, France* (JACoW, Geneva, Switzerland, 2013), p. 1212.

[30] H. Li, A. Miyazaki, M. Zhovner, L. Hermansson, R. Santiago Kern, K. Fransson, K. Gajewski, and R. Ruber, Progress and preliminary statistics for the ESS series spoke cryomodule test, in *Proceedings of SRF2021, East Lansing, MI* (JACoW, Geneva, Switzerland, 2021), p. 512.

[31] H. Li, A. Miyazaki, R. Santiago Kern, L. Hermansson, T. Lofnes, K. Gajewski, K. Fransson, R. Wedberg, and R. Ruber, RF performance of the spoke prototype cryomodule for ESS, FREIA Report No. 2019/08, 2019.

[32] H. Li, M. Jobs, R. Santiago Kern, V. A. Goryashko, L. Hermansson, A. Bhattacharyya, T. Lofnes, K. Gajewski, K. Fransson, and R. Ruber, Characterization of a $\beta = 0.5$ double spoke cavity with a fixed power coupler, Nucl. Instrum. Methods Phys. Res., Sect. A **927,** 63 (2019).

[33] R. Santiago Kern, C. Svanberg, K. Fransson, K. Gajewski, L. Hermansson, H. Li, T. Lofnes, M. Olvegå rd, I. Profatilova, M. Zhovner, A. Miyazaki, and R. Ruber, Completion of testing series double-spoke cavity cryomodules for ESS, in *Proceedings of the 21st International Conference on Radio-Frequency Superconductivity, SRF-2023, Grand Rapids, MI* (JACoW, Geneva, Switzerland, 2023), see also https://arxiv.org/abs/2306.11333.